Precise control of the global rotation of strongly coupled ion plasmas in a Penning trap

X.-P. Huang, J.J. Bollinger, T.B. Mitchell, and W.M. Itano
Time & Frequency Division, National Institute of Standards and Technology, Boulder, CO 80303

D.H.E. Dubin
Department of Physics, University of California at San Diego, La Jolla, CA 92093
(November 13, 1997)

Rotating asymmetric electric fields have been applied to control the rotation frequency (and hence the density) of nonneutral plasmas, which are confined in Penning-type traps and have relaxed close to thermal equilibrium characterized by a global rigid-body rotation. "Infinite" confinement times and density compression were first reported for uncorrelated plasmas of $\sim 10^8$ Mg^+ ions with temperatures ranging from 1 K to 5×10^4 K (4 eV) [Huang, *et al.*, Phys. Rev. Lett. **78**, 875 (1997)]. In this paper, we control strongly coupled plasmas of $\sim 10^5$ $^9Be^+$ ions which are laser-cooled to millikelvin temperatures so that the plasma freezes into a solid with a crystalline lattice. Here, Bragg diffraction peaks from crystals provide an accurate way of measuring the rotation frequency, and we observe that the plasma rotation can be phase-locked to the applied rotating field without any slip. In essence, these corotating plasmas have reached thermal equilibrium with the applied rotating field, and the azimuthally asymmetric boundaries of the equilibrium states have been measured experimentally. We use both rotating dipole and quadrupole fields to provide this precise control of the plasma rotation. However, the effectiveness of the dipole field depends on the presence of multiple ion species. With the rotating dipole field, density compression to near the Brillouin limit and increase of the rotation frequency to near the cyclotron frequency have been achieved.

PACS numbers: 52.25.Wz, 32.80.Pj,

I. INTRODUCTION

Unneutralized plasmas with a single sign of charge are often confined in Penning-type traps [1,2] for a variety of experiments including plasma physics [3], Coulomb crystal studies [4,5], precision spectroscopy [6,7], antimatter research [8,9], and storage of highly charged ions [10]. Since there is an average radial electric field, these trapped nonneutral plasmas undergo a global ($\mathbf{E} \times \mathbf{B}$) rotation about the magnetic field axis. In principle, perfect confinement can be obtained in an ideal trap with cylindrical symmetry due to conservation of (canonical) angular momentum [11]. In practice, background neutral molecules [12–14] and static field asymmetries [12,15–18] exert an ambient drag on the rotating plasma, causing slow expansion and eventual particle loss. Radiation pressure from laser beams has been used to balance the angular momentum loss and to vary the plasma rotation frequency [19,20]. However, this method is limited to the few ion species whose atomic transitions are accessible by a laser, and is not precise due to laser power, frequency, and pointing fluctuations. Recently, azimuthally asymmetric ("rotating wall") electric fields rotating in the same sense as the plasma have been used to exert a torque on Mg^+ plasmas with temperatures ranging from 1 K to 5×10^4 K (4 eV), resulting in steady-state confinement and density compression [21–23]. For these uncorrelated plasmas, the stabilized rotation frequency is somewhat less than that of the rotating field, with a slip frequency which increases with the plasma temperature [22].

In this report, we show that rotating wall electric fields applied to a Penning trap with quadratic potentials can control the rotation of laser-cooled, crystallized $^9Be^+$ plasmas without slip, thus extending the applicability of this technique from uncorrelated plasmas to strongly coupled systems [24]. Precise control of the plasma rotation is important for some applications. As an example, the second-order Doppler (time dilation) shift due to rotational velocity in a Penning trap atomic clock can be minimized by stabilizing the rotation at a particular frequency [7]. Both axially independent dipole and quadrupole fields in the plane perpendicular to the magnetic field have been used to provide this precise control of the plasma rotation. However, experimental evidences suggest that the effectiveness of the dipole field requires the presence of more than one ion species or other nonideal effects.

The rotating field control, which relies on ion-ion interactions, is fundamentally different from the sideband cooling or "axialization" techniques, where rf fields convert single-particle magnetron motion into damped axial or cyclotron motions [25–27]. The steady-state sideband-cooled radius of the magnetron motion depends on the strength of the rf field and the damping rate of the motion to which the magnetron motion is being coupled. In general, the rotation control will be of limited precision and may be effective only for low rotation frequencies where the space-charge field is weak [28]. In contrast, the rotating fields interact with ions near the plasma surface, creating a small-amplitude traveling wave. The torque due to this wave is then transferred to the plasma interior through "viscosity" or strong ion-ion Coulomb coupling,

which acts to bring the plasma to the same rotation frequency as the applied field [29].

In the present experiment, side-view images show that the plasma shape, which is determined by the rotation frequency, can be varied by gradually changing the rotating field frequency for both weakly and strongly coupled plasmas. When the plasma is sufficiently cold and crystalline lattices are formed, Bragg diffraction provides a more accurate measurement of the rotation frequency. It is observed that the lattice and its orientation can be stable for longer than 30 min ($\sim 10^8$ rotations), and its rotation can be phase-locked to the rotating field during this time. In essence, these co-rotating plasmas have reached a new kind of global thermal equilibrium [29], where the rotation frequency (and hence the density) is set precisely by the external drive. For the rotating quadrupole field, we have measured the triaxial ellipsoidal surface of this equilibrium state for oblate (pancake-like) plasmas, and found quantitative agreement with the analytical theory. For the rotating dipole field applied to plasmas with contaminant ions, we have observed the expected asymmetric distribution of the $^9Be^+$ ions in close agreement with Monte Carlo simulations. Control of the global rotation has been achieved for nearly all allowed rotation frequencies with the use of rotating dipole field.

II. EXPERIMENTAL SETUP

Figure 1 shows the apparatus with its optical diagnostics and schematics of the rotating dipole and quadrupole fields. The trap consists of a 127 mm long stack of cylindrical electrodes at room-temperature with an inner diameter of 40.6 mm, enclosed in a 10^{-8} Pa vacuum chamber. The uniform magnetic field $B_0 = 4.46$ T is aligned parallel to the trap axis within 0.01°, giving a $^9Be^+$ (charge e and mass m) cyclotron frequency $\Omega = eB_0/m = 2\pi \times 7.61$ MHz. An axisymmetric trapping potential $(m\omega_z^2/2e)[z^2 - (x^2 + y^2)/2]$ is generated near the trap center by biasing the central electrodes to a negative voltage $-V_0$. At $V_0 = 1$ kV, the single-particle axial frequency $\omega_z = 2\pi \times 799$ kHz and the magnetron frequency $\omega_m = (\Omega - \sqrt{\Omega^2 - 2\omega_z^2})/2 = 2\pi \times 42.2$ kHz. The z-independent rotating fields are generated by applying properly phased sinusoidal voltages of amplitude V_w to the 6-fold azimuthal sectors of the two compensation electrodes, which are positioned symmetrically in the axial direction with respect to the trap center.

We create $^9Be^+$ plasmas by ionizing neutral ^9Be atoms in a separate trap (not shown) and then transferring the ions to the main trap for experimentation [20]. This procedure can be repeated several times to accumulate up to 10^6 ions. We expect that essentially all the ions in the trap are singly charged since the formation of doubly charged ions is energetically forbidden. While the total charge in the trap is conserved after loading, the relative abundance of contaminant ions increases from $< 5\,\%$ for a new cloud on a timescale of 20 hours, presumably due to reactions between $^9Be^+$ ions and background neutral molecules. By exciting ion cyclotron resonances, we determine that the two main contaminant ion species have mass 10 u and 26 u, where u is the atomic mass unit. These two species are likely to be BeH^+ and $BeOH^+$, respectively. Unless noted, data presented in this paper are obtained on relatively clean clouds with $< 10\,\%$ contaminant ions.

The trapped $^9Be^+$ ions are Doppler-cooled by two laser beams tuned slightly below the $2s\,^2S_{1/2}(M_I = 3/2, M_J = 1/2) \rightarrow 2p\,^2P_{3/2}(3/2, 3/2)$ resonant transition frequency (wavelength $\lambda \approx 313.11$ nm) [19]. These laser beams also optically pump most of the ions into the $2s\,^2S_{1/2}(3/2, 1/2)$ state. ¿From previous experiments [19,20], we estimate that temperatures $T \lesssim 10$ mK can be obtained. Here, $k_B T$ refers to the average ion thermal energy in a frame rotating with the plasma, which is typically much smaller than the average kinetic energy in the global rotation ($\sim 10^2$ K). The axial cooling beam (waist diameter ≈ 0.5 mm, power $\approx 50\,\mu$W), directed parallel to $\mathbf{B_0}$ as shown in Fig. 1, cools the ion thermal motion while not affecting the global rotation. A second laser beam (not shown in Fig. 1) with a much smaller waist diameter (≈ 0.07 mm) is directed perpendicular to $\mathbf{B_0}$ and is used to compress the plasma and vary the rotation frequency. This beam is turned off during the Bragg scattering measurements.

When the cloud reaches thermal equilibrium at these cryogenic temperatures, the plasma Debye length becomes much smaller than its diameter $2r_0$ and axial length $2z_0$. The influence of image charges is negligible here due to the small dimensions of the plasma compared to the trap radius ($< 10\,\%$). Consequently, the plasma forms a uniform density spheroid, bounded by $z^2/z_0^2 + (x^2 + y^2)/r_0^2 = 1$, with a rigid-body rotation frequency ω_r in the range $\omega_m < \omega_r < (\Omega - \omega_m)$ [20]. The particle density n_0 is determined from ω_r according to $\omega_p^2 \equiv e^2 n_0/\epsilon_0 m = 2\omega_r(\Omega - \omega_r)$, where ω_p is the plasma frequency [20]. The maximum density (Brillouin limit) $n_B \equiv \epsilon_0 B_0^2/2m = 5.9 \times 10^9\,\mathrm{cm}^{-3}$ occurs at $\omega_r = \Omega/2$, the condition for Brillouin flow. In the frame rotating with the plasma, (x_r, y_r, z), the $e\,\mathbf{v}\times\mathbf{B}$ Lorentz force gives rise to a radially confining pseudo-potential, and the effective vacuum trapping potential becomes

$$\Phi_r = \frac{m\omega_z^2}{2e}[z^2 + \beta(x_r^2 + y_r^2)]\,, \qquad (1)$$

where β is the radial trapping strength defined as

$$\beta \equiv \frac{1}{2}\left(\frac{\omega_p^2}{\omega_z^2} - 1\right) = \frac{\omega_r(\Omega - \omega_r)}{\omega_z^2} - \frac{1}{2} > 0\,. \qquad (2)$$

The parameter β determines the aspect ratio $\alpha \equiv z_0/r_0$ of the spheroid [20,29]. We use an f/5 imaging system to

detect resonantly scattered photons from the axial cooling beam and produce a side-view image of the $^9Be^+$ ions. ¿From this side-view image, we measure α and obtain ω_r and n_0.

For the typical conditions of $T \lesssim 10\,\mathrm{mK}$ and $n_0 \gtrsim 4\times10^8\,\mathrm{cm}^{-3}$, we obtain a Coulomb coupling parameter

$$\Gamma \equiv \left(\frac{e^2}{4\pi\epsilon_0\, a_{\mathrm{WS}}}\right)\frac{1}{k_{\mathrm{B}}T} > 200\,, \tag{3}$$

where the Wigner-Seitz radius a_{WS} is defined by $4\pi a_{\mathrm{WS}}^3/3 \equiv n_0^{-1}$. This strong ion-ion coupling results in the formation of crystalline lattices, which are body-centered cubic (bcc) in nearly spherical plasmas ($\alpha \approx 1$) with ion number $N \gtrsim 2\times10^5$ [4,5]. As shown in Fig. 1, Bragg-scattered light from the axial cooling beam is detected with a charge-coupled device (CCD) camera near the forward-scattering direction since the wavelength is much smaller than the lattice spacing ($\lambda \ll a_{\mathrm{WS}}$) [4]. After passing through the trap, the axial cooling beam is deflected away from the lenses collecting the Bragg scattered light.

III. RESULTS AND ANALYSES

A. General results for both rotating fields

When the rotating fields are first applied, their rotation frequency ω_w is set close to ω_r so that they interact strongly with the plasma. By measuring the photon scattering rate from the cooling beams for a fixed laser frequency, which is a function of the ion temperature, we have established that the ion temperature does not change significantly with the application of the rotating fields. Since the rotating fields typically cause less than 1 % shape distortion to the plasma (see later discussions), the plasma rotation frequency ω_r can still be inferred from the aspect ratio α within the 5 % uncertainty of this method. Furthermore, because Φ_r depends weakly on the ion mass for $\omega_r \ll \Omega/2$ as shown in Eq. (2), a multi-species plasma essentially has the same charge distribution as a pure $^9Be^+$ plasma except for the effect of centrifugal separation, in which the heavier ions tend to occupy positions at larger radii [30]. With a sufficiently large rotating field amplitude V_w, we are able to vary the plasma aspect ratio (and hence ω_r) by gradually changing ω_w. Figure 2 shows ω_r as determined from the side-view images versus ω_w with both the rotating dipole and quadrupole fields and for several plasmas with $N < 7\times10^4$ and $\omega_r \ll \Omega/2$. The plasma rotation frequency ω_r tracks ω_w closely within the experimental accuracy, demonstrating external control of the plasma rotation by the rotating fields. The data of Fig. 2 were obtained at low temperatures ($T \lesssim 10\,\mathrm{mK}$) with the axial cooling laser on continuously. However, we are also able to control the plasma rotation with the laser tuned far below the atomic transition frequency or blocked for short periods of time ($\sim$1 min). Under these conditions, we expect a significantly higher plasma temperature ($T \sim 10\,\mathrm{K}$) so that the plasma is only weakly correlated.

For a more accurate determination of ω_r, we use the time dependence of the laser light Bragg-scattered from the rotating crystals [4,5]. A gateable image intensifier, installed in front of the CCD camera, allows the diffraction pattern to be recorded stroboscopically. Figure 3(a) shows a time-averaged diffraction pattern of concentric rings from an approximately spherical plasma with $N \approx 7.5\times10^5$. Even if this pattern is from a single crystal, rings are observed because of the plasma rotation about the axial laser beam [4]. With the rotating field applied and controlling the plasma rotation, we trigger the intensifier synchronously with the rotating field opening the camera for 50 ns each $2\pi/\omega_w$ period. This enables the camera to record the diffraction pattern in the rest frame of the rotating field. Figure 3(b) shows such a time-resolved pattern taken nearly simultaneously with Fig. 3(a) and accumulated over $\sim10^6$ plasma rotations. The well-defined rectangular dot pattern demonstrates that the crystal is phase-locked to the rotating field. In this work, we could determine phase-locked rotation when $\mathbf{B_0}$ is aligned within 0.01° of the trap axis and for $\omega_r \lesssim \Omega/20$. This alignment is obtained by minimizing the amplitude of zero frequency modes of the plasma [2]. Furthermore, the structure and spacing of the crystalline lattice and its orientation with respect to the laser beam can last longer than 30 min under this rotation control. For comparison, a particular Bragg scattering pattern typically lasts for $\sim$1 min without the rotating field control, perhaps due to effects from the plasma spin-down. With a weak rotating field amplitude or when the trap axis is tilted a few hundredth of a degree with respect to $\mathbf{B_0}$, we cannot obtain phase locking but are able to stabilize the plasma rotation frequency close to the rotating field frequency with $\lesssim$1 % slippage.

B. Quadrupole field control

With the rotating quadrupole field, which has a potential $\propto (y^2-x^2)\cos(2\omega_w t) + 2xy\sin(2\omega_w t)$, the equilibrium plasma surface is actually a spinning triaxial ellipsoid with three principal axes differing in length [29]. Since the plasma is phase-locked with $\omega_r = \omega_w$, the combined vacuum trapping potential in the rotating frame becomes

$$\Phi_r' = \frac{m\omega_z^2}{2e}[z^2 + (\beta-\delta)x_r^2 + (\beta+\delta)y_r^2]\,, \tag{4}$$

where $\delta = f_g\, V_w/V_0 \geq 0$ is the relative strength of the quadrupole field and f_g depends only on the trap geome-

try. The thermal equilibrium state in the frame rotating with the plasma is bounded by $z^2/z_0^2+x_r^2/x_0^2+y_r^2/y_0^2=1$ with $x_0 \geq y_0$. The parallel and perpendicular aspect ratios ($\alpha_\parallel \equiv z_0/y_0$, $\alpha_\perp \equiv x_0/y_0$) are determined by parameters β and δ [29]. This shape produces a space-charge potential which cancels Φ_r' within the equilibrated plasma. In this equilibrium, each individual ion still undergoes a purely rotational average motion in the same way as the ordinary thermal equilibrium state without the rotating field.

To obtain an $\alpha_\perp$ significantly above one, we maximize the ratio δ/β by reducing V_0 to less than 200 V and setting ω_w close to the magnetron frequency ω_m. At these low rotation frequencies and with only the perpendicular cooling beam, the contaminant ions are well mixed with the $^9Be^+$ ions, making the boundary of the fluorescing $^9Be^+$ ions coincide with that of the plasma. Side-view images of the plasma are then recorded stroboscopically at different phases of the rotating field. In the laboratory frame, the plasma radius $r_{\rm lab}$ is expected to oscillate at $2\omega_w$, with an amplitude proportional to $x_0 - y_0$. Figure 4 shows a measurement of $r_{\rm lab}$ on a plasma with $\alpha_\parallel \approx 0.15$ and $\alpha_\perp \approx 1.4$, rotating at 2.5 kHz ($V_0 = 50$ V, $V_w \approx 185$ V). Excellent agreement between the theory and data is exhibited, showing that the plasma is indeed equilibrated with the rotating quadrupole field.

We have measured the dependence of $\alpha_\perp$ on parameters δ and β. Figure 5(a) shows $\alpha_\perp$ versus δ at fixed $\beta = 0.103$. Good agreement with the theory is obtained by fitting these data for f_g with the result $f_g \approx 6.38 \times 10^{-3}$. Figure 5(b) shows $\alpha_\perp$ versus β for fixed $\delta \approx 0.0159$ using the calibrated f_g value. Excellent agreement is again observed, showing the rapid decrease to unity for $\alpha_\perp$ as β is increased. Under typical conditions ($V_0 \geq 500$ V, $V_w \leq 50$ V, and $\omega_w \geq 1.1\omega_m$, giving $\delta < 7 \times 10^{-4}$ and $\beta > 0.1$), $\alpha_\perp - 1$ is less than 1 %. This small distortion, however, generates sufficient torque to phase-lock the plasma rotation.

C. Dipole field control

We have examined rotation control using the dipole field with a potential $\propto y\sin(\omega_w t) - x\cos(\omega_w t)$. Theoretically, this field is not expected to provide rotation control for a single-species plasma in a quadratic trap. Instead, it drives only a "center-of-mass" orbital motion about the trap axis without surface distortions and is decoupled from the internal plasma rotation. Experimentally, however, rotation control including phase locking similar to that from the quadrupole field is obtained with the rotating dipole field as discussed in the previous sections. While the asymmetric field from image charges induced by the center-of-mass motion could provide the observed coupling to the plasma rotation, this field is too weak to be effective for our typical trap parameters.

Experimental evidences suggest that the coupling between the center-of-mass motion and plasma rotation is provided by the contaminant ions. By measuring the plasma dynamic response under sudden changes of the dipole field frequency [22], we have observed that the torque from the dipole field increases with time, presumably due to the growing percentage of the contaminant ions. Figure 6 shows the evolution of plasma rotation frequency as ω_w is suddenly changed by ± 5 kHz from 60 kHz (magnetron frequency $\omega_m = 2\pi \times 42.2$ kHz) at $\Delta t = 0$. The initial and final rotation frequencies of the plasma are equal to that of the dipole field as determined from time-resolved Bragg scattering measurements. The intermediate data points are derived from the aspect ratio of the side-view images assuming that the plasma goes through successive thermal equilibrium states during the evolution. The torque from the rotating dipole field has clearly increased from the one-hour-old plasma with approximately 5 % contaminant ions to the two-hour-old plasma with twice as many contaminant ions.

The effect of the contaminant ions on the plasma can be understood in terms of their azimuthally asymmetric distribution with the rotating dipole field. For typical rotation frequencies and laser cooling conditions, these heavier contaminant ions separate radially from the $^9Be^+$ ions and form a nonfluorescent outer cylindrical layer without the rotating field [30,31]. As the plasma undergoes a driven center-of-mass circular motion with the rotating dipole field, the contaminant ions distribute preferentially away from the trap center. This asymmetric distribution of the contaminant ions with respect to the $^9Be^+$ ions produces a coupling between the driven center-of-mass motion and the plasma rotation, enabling the rotating dipole field control. When the plasma reaches thermal equilibrium with the rotating dipole field with $\omega_r = \omega_w$, the average ion motion is simply a rigid-body rotation about the *trap* axis at ω_w.

Figure 7 shows the radial boundary position $x_{\rm Be}$ (at $z = 0$) of a plasma containing about 12 % contaminant ions and phased-locked with a dipole field rotating at 9 kHz (trap magnetron frequency is 8.4 kHz). This measurement is obtained from time-resolved side-view images with the same technique that was used for the quadrupole field results. For this measurement, however, the contaminant ions are well separated from the $^9Be^+$ ions due to the higher rotation frequency. For a pure $^9Be^+$ plasma, a periodic oscillation at ω_w is expected in the laboratory frame due to the center-of-mass motion, as shown in Fig. 7. The data generally follow this prediction except for the "clipping" of $x_{\rm Be}$ at certain phases of the rotating dipole field.

A Monte Carlo simulation on the equilibrium distribution of a two-species plasma (in the rest frame of the dipole field) is shown in Fig. 8. The plasma is made of 1000 particles with 88 % $^9Be^+$ (dots) and 12 % contaminant ions having mass 26 u (open circles), and is

driven by a rotating dipole field resulting in the same relative displacement as in Fig. 7. The plasma has a very oblate shape to enhance its center-of-mass displacement as shown in the side-view of Fig. 8(b). In the x-y distribution shown in Fig. 8(a), the overall charge is distributed nearly symmetrically with respect to the shifted plasma axis, while the $^9Be^+$ ions and the contaminant ions are positioned asymmetrically inside the plasma. The boundary of the $^9Be^+$ ions is approximately made of two arcs: one, bordering the vacuum is centered on the plasma axis (the $\oplus$ symbol), and the other, bordering the contaminant ions is centered on the trap axis (the cross). This shape explains the observed clipping of $x_{\rm Be}$ in Fig. 7. The small discrepancy between the data and the solid curve in Fig. 7 is likely due to an overestimate of the percentage of the contaminant ions from the side-view images without the rotating field.

When contaminant ions are present, it is advantageous to use the dipole rather than quadrupole field to control the plasma rotation because greater electric field strength at the plasma surface can be obtained for the same amplitude V_w on the compensation electrodes. This is because the plasma dimensions are typically much smaller than the trap radius and the dipole field decays much more slowly from the compensation electrodes than the quadrupole field. Rotation control in the range $\omega_m < \omega_r < (\Omega - \omega_m)$, which includes rotational equilibrium near the Brillouin flow, has been achieved using the rotating dipole field. In the rotation frequency regime $\omega_r \sim \Omega/2$, crystalline lattices are generally not observed, and the aspect-ratio α depends only weakly on the rotation frequency. However, we can infer ω_r by measuring the angle $\theta_{\rm scatt}$ of the first Bragg scattering ring from ions in the shell structures. This angle is related to $a_{\rm WS}$ [4], hence giving the plasma density and rotation frequency. Figure 9 shows the scattering angle $\theta_{\rm scatt}$ as a function of the rotation frequency of the dipole field for two plasmas with different composition of contaminant ions. With only heavier contaminant ions (dots), we can control the plasma rotation frequency up to about $0.9\,\Omega$ (dotted vertical line) corresponding to the frequency at which BeH^+ ions can no longer remain in the plasma. If we intentionally create some lighter ions (crosses), we are able to control ω_r throughout all allowed rotation frequencies. This observation provides further evidence that the contaminant ions are the main coupling mechanism for the rotating dipole field. We cannot, however, exclude the possibility that different nonideal effects can cause sufficient coupling in other experiments.

IV. CONCLUSIONS AND DISCUSSION

We have shown experimentally that azimuthally asymmetric electric fields rotating in the same sense as the plasma can exert a torque that balances the ambient drag in both weakly and strongly coupled regimes, resulting in infinite confinement times. The torque from the rotating wall fields acts to bring the plasma to the same rotation frequency as the applied field. For strongly coupled plasmas with laser-cooling, we obtain phase-locked rotation with the rotating field, therefore enabling precise control of plasma properties such as density and aspect ratio in Penning traps with quadratic potentials. Both z-independent dipole and quadrupole rotating fields are used in this experiment, although the effectiveness of the dipole field depends on the presence of more than one ion species.

There may be other methods to inject angular momentum into the plasma and vary the rotation frequency. For example, by exciting an azimuthally asymmetric mode that travels in the same direction but faster than the plasma rotation, ω_r can be increased very effectively due to the global coherent resonance [16,32]. The challenge of this approach is to remain on resonance with the mode as the plasma rotation frequency is increased. It may also be difficult to balance the heating from the mode excitation. In addition, this method will probably not result in rotation control as precise as the rotating field technique.

Substantial questions remain concerning the theoretical models which give quantitative predictions for the torque from the rotating fields [33,34]. In the strongly coupled regime, such models that describe the experiment are lacking. For uncorrelated plasmas at higher temperatures, two-dimensional rotating fields may not be able to generate enough torque to balance the ambient drag, and electric fields with nonzero z-components may be required [22]. Rotating field control of pure electron plasmas also needs further refinement to improve its capability [23].

In the future, direct imaging of individual ions in a crystallized plasma may be possible because of the phase-locked rotation. In addition, the increased crystal stability improves the prospect of observing the predicted solid–liquid phase transition of strongly coupled plasmas. Dynamics of the Brillouin flow is also an interesting area for investigation. Finally, it may be possible to influence the formation of crystalline lattices with the rotating fields and other perturbations, enabling external control of the crystal orientation.

V. ACKNOWLEDGEMENTS

We thank D. Wineland, T. O'Neil, and C.F. Driscoll for discussion, and B. Jelenković, R. Rafac, M. Young, M. Lombardi, and D. Sullivan for useful comments on the manuscript. This work is supported by the Office of Naval Research.

[1] J.H. Malmberg, C.F. Driscoll, B. Beck, D.L. Eggleston, J. Fajans, K. Fine, X.-P. Huang, and A.W. Hyatt, in *Non-neutral Plasma Physics*, edited by C.W. Roberson and C.F. Driscoll (AIP, New York, 1988), p. 28.

[2] J.J. Bollinger, D.J. Wineland, and D.H.E. Dubin, Phys. Plasmas **1**, 1403 (1994).

[3] For recent results, see *Non-neutral Plasma Physics II*, edited by J. Fajans and D.H.E. Dubin (AIP, New York, 1995).

[4] J.N. Tan, J.J. Bollinger, B. Jelenkovic, and D.J. Wineland, Phys. Rev. Lett. **75**, 4198 (1995); J.N. Tan, J.J. Bollinger, B. Jelenkovic, W.M. Itano, and D.J. Wineland, in *Physics of Strongly Coupled Plasmas*, edited by W.D. Kraeft and M. Schlanges (World Scientific, Singapore, 1996), p. 387.

[5] W.M. Itano, J.J. Bollinger, J.N. Tan, B. Jelenkovic, X.-P. Huang, and D.J. Wineland, "Bragg diffraction from crystallized ion plasmas," submitted to Science (1997).

[6] R. Blatt, P. Gill, and R.C. Thompson, J. Mod. Opt. **39**, 193 (1992); R.C. Thompson, Adv. At. Mol. Phys. **31**, 63 (1993).

[7] J.N. Tan, J.J. Bollinger, and D.J. Wineland, IEEE Trans. Instrum. Meas. **44**, 144 (1995).

[8] G. Gabrielse, X. Fei, L.A. Orozco, R.L. Tjoelker, J. Hass, H. Kalinowsky, T.A. Trainer, and W. Kells, Phys. Rev. Lett. **65**, 1317 (1990).

[9] R.G. Greaves and C.M. Surko, Phys. Plasmas **4**, 1528 (1997).

[10] D. Schneider, D.A. Church, G. Weinberg, A.J. Steiger, B. Beck, J. McDonald, E. Magee, and D. Knapp, Rev. Sci. Instrum. **65**, 3472 (1994).

[11] T.M. O'Neil, Phys. Fluids **23**, 2216 (1980).

[12] J.S. deGrassie and J.H. Malmberg, Phys. Fluids **23**, 63 (1980).

[13] D.A. Moore, R.C. Davidson, S.M. Kaye, and S.F. Paul, in *Non-neutral Plasma Physics II* (Ref. [3]), p. 118.

[14] Torques from *rotating* neutral gas are considered in A.J. Peurrung and S.E. Barlow, Phys. Plasmas **3**, 2859 (1996).

[15] J.H. Malmberg and C.F. Driscoll, Phys. Rev. Lett. **44**, 654 (1980); C.F. Driscoll, K.S. Fine, and J.H. Malmberg, Phys. Fluids **29**, 2015 (1986).

[16] D.L. Eggleston, T.M. O'Neil, and J.H. Malmberg, Phys. Rev. Lett. **53**, 982 (1984).

[17] J. Notte and J. Fajans, Phys. Plasmas **1**, 1123 (1994).

[18] D.L. Eggleston, Phys. Plasmas **4**, 1196 (1997).

[19] J.J. Bollinger and D.J. Wineland, Phys. Rev. Lett. **53**, 348 (1984).

[20] L.R. Brewer, J.D. Prestage, J.J. Bollinger, W.M. Itano, D.J. Larson, and D.J. Wineland, Phys. Rev. A **38**, 859 (1988); D.J. Heinzen, J.J. Bollinger, F.L. Moore, W.M. Itano, and D.J. Wineland, Phys. Rev. Lett. **66**, 2080 (1991).

[21] Some preliminary results on Mg^+ plasmas are in F. Anderegg, X.-P. Huang, C.F. Driscoll, G.D. Severn, and E. Sarid, in *Non-neutral Plasma Physics II* (Ref. [3]), p. 1.

[22] X.-P. Huang, F. Anderegg, E.M. Hollmann, C.F. Driscoll, and T.M. O'Neil, Phys. Rev. Lett. **78**, 875 (1997).

[23] A preliminary work on pure electron plasmas is in R.E. Pollock and F. Anderegg, in *Non-neutral Plasma Physics II* (Ref. [3]), p. 139.

[24] X.-P. Huang, J.J. Bollinger, T.B. Mitchell, and W.M. Itano, "Phase-locked rotation of crystallized non-neutral plasmas by rotating electric fields," accepted for publication in Phys. Rev. Lett. (1997).

[25] D.J. Wineland and H.G. Dehmelt, Int. J. Mass Spec. Ion Proc. **16**, 338 (1974); erratum **19**, 251 (1976).

[26] L.S. Brown and G. Gabrielse, Rev. Mod. Phys. **58**, 233 (1986).

[27] G. Savard, St. Becker, G. Bollen, H.-J. Kluge, R.B. Moore, Th. Otto, L. Schweikhard, H. Stolzenberg, and U. Wiess, Phys. Lett. A **158**, 247 (1991); S. Guan, X. Xiang, and A.G. Marshall, Int. J. Mass Spec. Ion Proc. **124**, 53 (1993).

[28] C.S. Weimer, J.J. Bollinger, F.L. Moore, and D.J. Wineland, Phys. Rev. A **49**, 3842 (1994).

[29] D.H.E. Dubin and T.M. O'Neil, "Trapped nonneutral plasmas, liquids, and crystals (the thermal equilibrium states)," submitted to Rev. Mod. Phys. (1997).

[30] T.M. O'Neil, Phys. Fluids **24**, 1447 (1981).

[31] D.J. Larson, J.C. Bergquist, J.J. Bollinger, W.M. Itano, and D.J. Wineland, Phys. Rev. Lett. **57**, 70 (1986).

[32] T.B. Mitchell, Ph.D. thesis, University of California at San Diego (1993), p. 58.

[33] S.M. Crooks and T.M. O'Neil, Phys. Plasmas **2**, 355 (1995); S.M. Crooks, Ph.D. thesis, University of California at San Diego (1995), p. 56.

[34] R. Fitzpatrick and E.P. Yu, Phys. Plasmas **4**, 917 (1997).

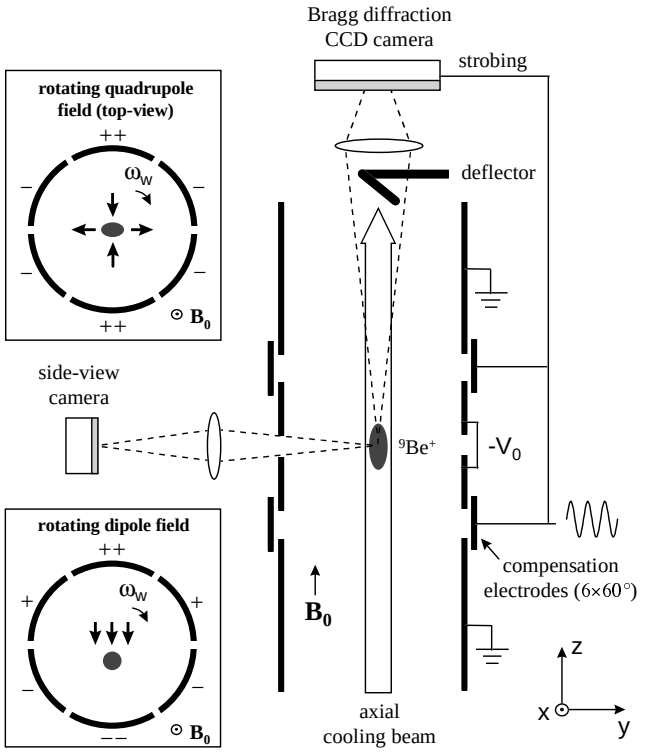

FIG. 1. Schematic side-view of the cylindrical trap with real-space imaging optics and Bragg diffraction detection system. Cross sections of the rotating dipole and quadrupole field (in the x-y plane) are shown separately in the two insets.

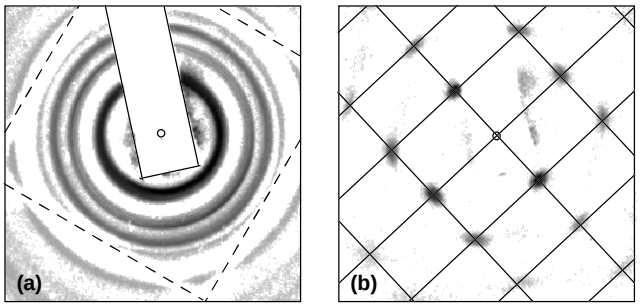

FIG. 3. Bragg diffraction patterns from a plasma phase-locked to a rotating quadrupole field ($\omega_r = \omega_w = 2\pi \times 140\,\mathrm{kHz}$, $n_0 \approx 4.26 \times 10^8\,\mathrm{cm}^{-3}$, $\alpha \approx 1.1$). (a) 1 s time-averaged pattern. The long rectangular shadow is from the deflector for the incident beam; four line shadows that form a square are due to a wire mesh at the exit window of the vacuum chamber. (b) Time-resolved pattern by strobing the camera with the rotating field (integration time ≈ 5 s). A spot is predicted at each intersection of the rectangular grid lines for a bcc with a {110} plane $\perp$ to the axial laser beam. The grid spacing is determined from n_0 and is not a fitted parameter.

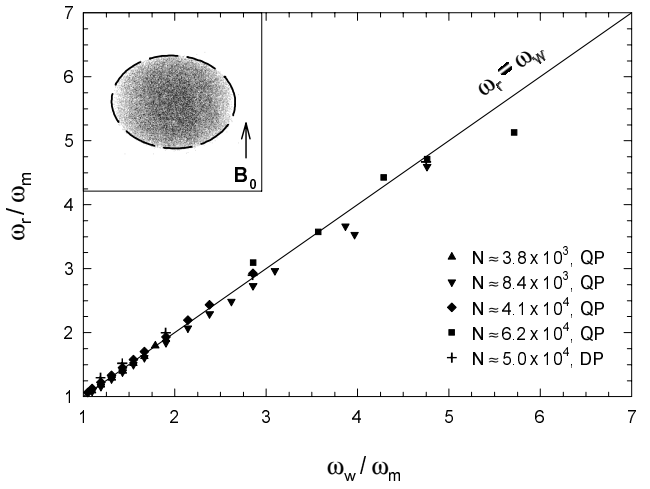

FIG. 2. The plasma rotation frequency ω_r versus the rotation frequency ω_w of the rotating fields. The frequency ω_r is determined from the aspect ratio α of several plasmas with $200 \le V_0 \le 1\,\mathrm{kV}$. Solid symbols are with the quadrupole field and crosses are with the dipole field. The inset shows a typical side-view image and its boundary fit to an ellipse (dashed line), giving α and ω_r.

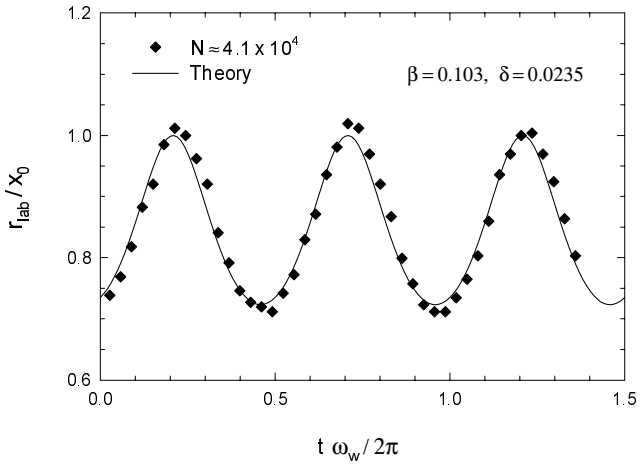

FIG. 4. Oscillation of the plasma radius r_{lab} in 1.5 rotation periods with the rotating quadrupole field. The theory curve is calculated using the calibrated f_g from Fig. 5(a). The relative phase between the theory and data is not adjusted.

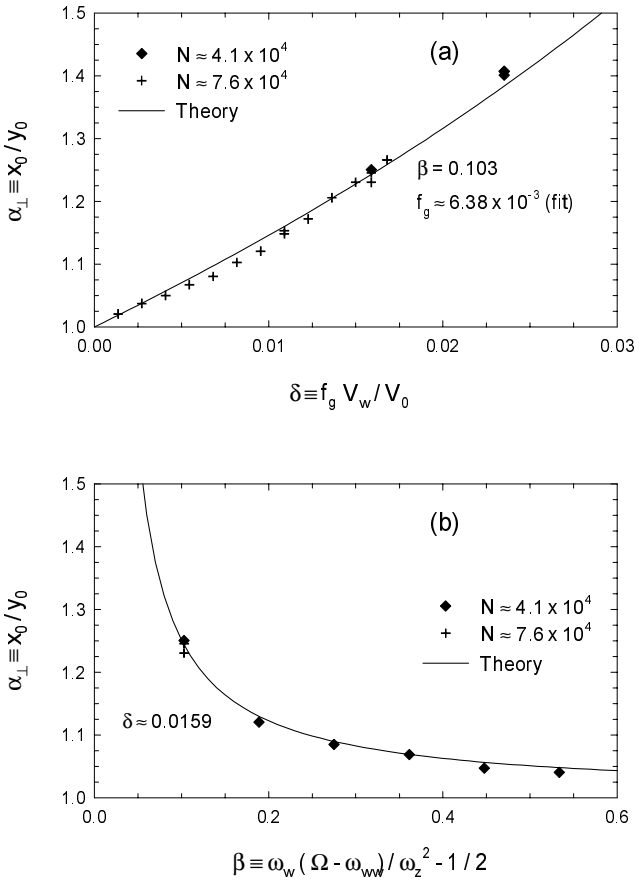

FIG. 5. Dependence of perpendicular aspect ratio $\alpha_\perp$ versus (a) rotating field strength δ and (b) radial trapping strength β. Two plasmas are used with $50 \leq V_0 \leq 100\,\mathrm{V}$ and $15 \leq V_w \leq 185\,\mathrm{V}$. The geometric factor f_g is calibrated in (a).

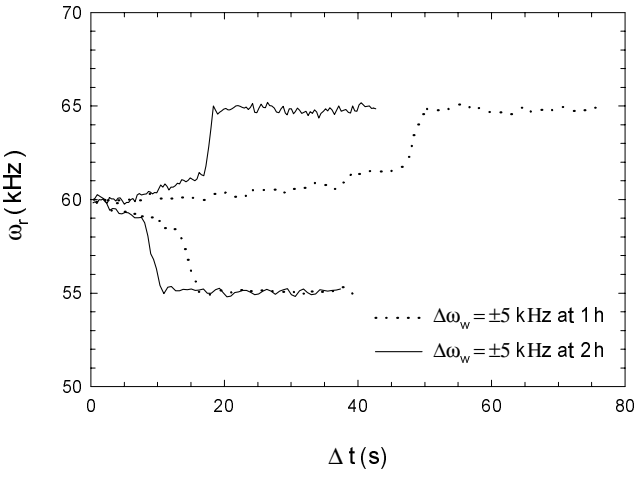

FIG. 6. Time evolution of the plasma rotation frequency under sudden changes of the dipole field frequency. Measurements on the same plasma at two times are plotted.

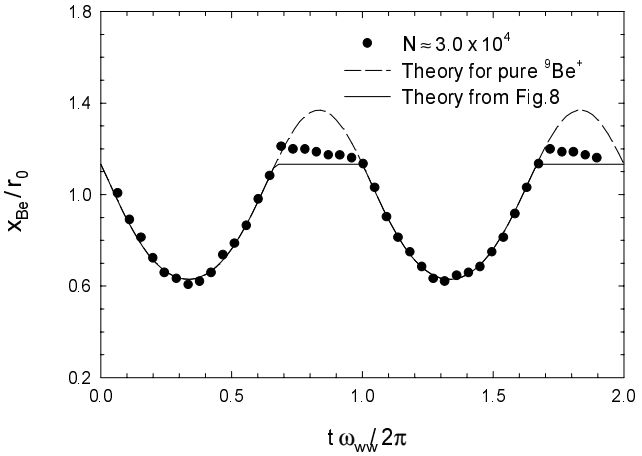

FIG. 7. Oscillation of the $^9Be^+$ radial boundary position x_{Be} in 2 rotation periods with the rotating dipole field. The dashed curve is calculated for a pure $^9Be^+$ plasma and the solid curve is obtained from the simulation shown in Fig. 8. The dipole field amplitude at the plasma is obtained by fitting the data, while the relative phase between the theories and data is not adjusted.

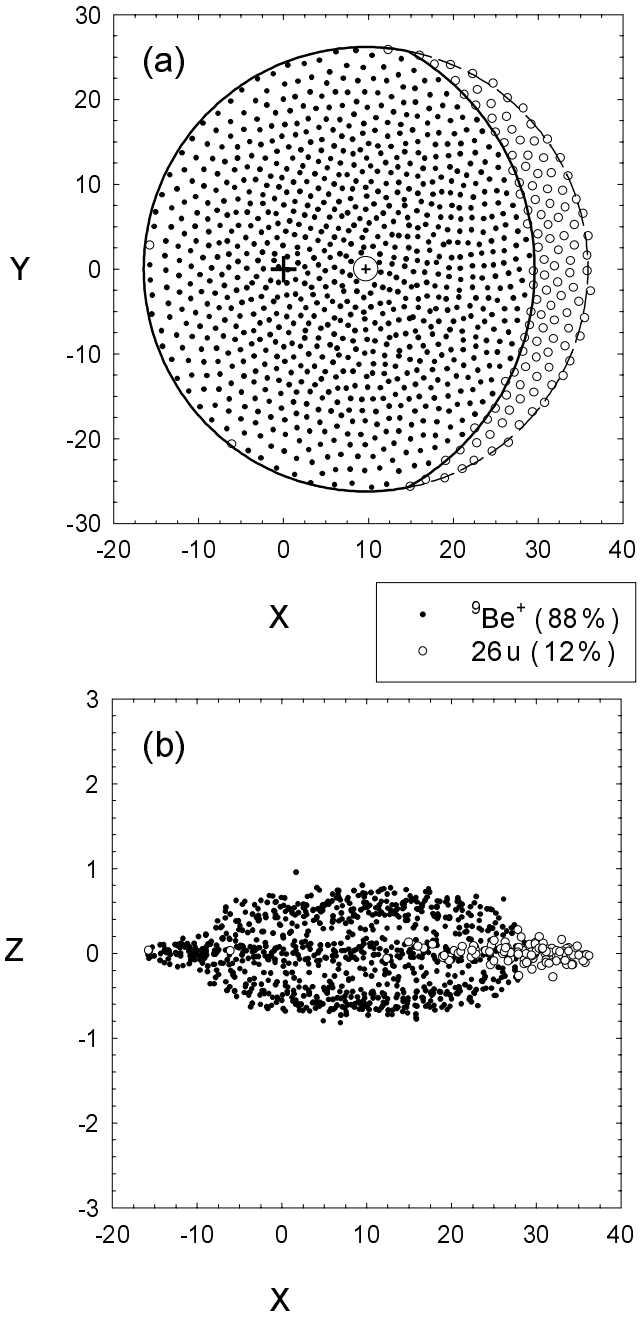

FIG. 8. A Monte Carlo simulation of the thermal equilibrium distribution of a two-species plasma with the rotating dipole field. The plasma is made of 1000 particles with 88 % $^9Be^+$ and 12 % contaminant ions having mass 26 u, and has a coupling parameter $\Gamma = 40$. The trapping parameters are the same as in Fig. 7. (a) The x-y distribution. Solid and dashed lines denote boundaries of the $^9Be^+$ ions and the plasma respectively. (b) The x-z distribution with ten times smaller z scale.

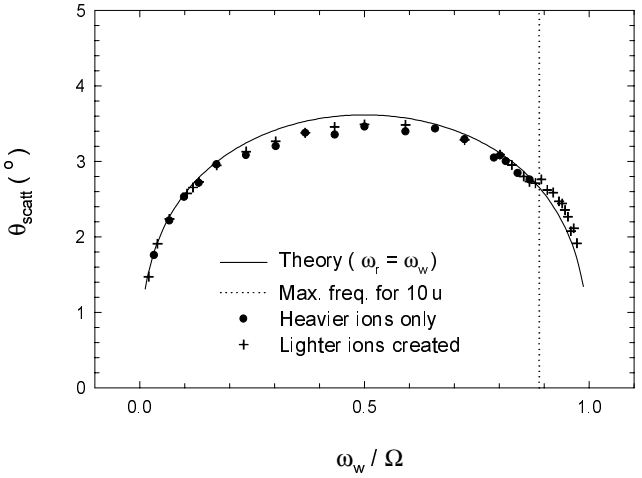

FIG. 9. The angle of the first Bragg scattering ring from shells versus the rotation frequency of the dipole field. Data from a plasma with only heavier contaminant ions are shown as dots. Crosses are data from a plasma with some lighter ions than $^9Be^+$.